

The Radial Dependence of Temperature and Iron Abundance Galaxy Clusters from $z=0.14$ to $z=0.89$

Steven Ehlert^{1,3} and M. P. Ulmer^{2,3}

¹ Max-Planck-Institut für Kernphysik, PO Box 103980, 69029 Heidelberg, Germany email: Steven.Ehlert@mpi-hd.mpg.de

² LAM, Pôle de l'Etoile Site de Château-Gombert, 38, rue Frédéric Joliot-Curie, 13388 Marseille Cedex 13, France email:m-ulmer2@northwestern.edu

³ Department of Physics and Astronomy, Northwestern University, 2131 Sheridan Road, Evanston, IL 60208-2900, USA

Received March 18, 2008, Accepted June 6, 2009

ABSTRACT

Context. The origin and evolution of the intracluster medium (ICM) are still not fully understood. A better understanding is not only interesting in its own right, but it is also important for modeling hierarchical structure growth and for using cluster surveys to determine cosmological parameters.

Aims. To determine if there exists any evidence for evolution in the temperature or iron abundance gradients between $z \approx 0.14$ and $z \approx 0.89$, therefore elucidating the origin of energy and metal input to the ICM.

Methods. By using a sample of 35 observations of 31 clusters of galaxies found in the archival data of *Chandra* and *XMM-Newton* with redshifts between 0.14 and 0.89, we derived the temperature and iron abundance radial profiles. To compare clusters with similar properties, the data were divided into comparable subsets.

Results. There is no substantial evidence to suggest that the iron abundance radial profiles in galaxy clusters evolve with redshift in any of the chosen subsets. Temperature radial profiles also do not appear to be changing with redshift once selection effects are taken into account.

Conclusions. The lack of evolution in the iron profiles is consistent with scenarios where the galaxies in clusters are stripped of their gas at higher redshifts. The temperature and iron abundance profiles also suggest that the primary source of heating in high redshift clusters is the gravitational infall of mass. These findings further emphasize the importance of modeling the local environment of clusters in cosmological studies and have important implications for studies that go to larger redshifts.

Key words. X-rays: galaxies: clusters

1. Introduction

Many dynamic processes occur in the high temperature, iron rich intracluster medium (ICM) of rich clusters of galaxies. Radiative cooling, supernova driven winds, and ram pressure stripping are just a few of the processes by which thermal energy and iron may be injected into the ICM. The theory of these processes is discussed in detail elsewhere (e.g., Sarazin 1988; Rosati et al. 2002; Arnaud 2005). In order to help resolve which processes most significantly contribute to the heating and iron enrichment within clusters, the location and evolution with redshift of both iron abundance and thermal energy can be used to provide significant clues.

Both *Chandra* and *XMM-Newton* have the angular resolution to make two-dimensional maps for nearby clusters such as Coma and Perseus (e.g., Fabian et al. 2006), but the statistical significance of the archival data is not generally sufficient for these types of measurements in distant clusters.

Many have already investigated how overall temperatures or iron abundances might vary with redshift, including Balestra et al. (2007), Bonamente et al. (2006), Tozzi et al. (2003), and Sanderson et al. (2006). So far

very little evidence for the evolution of the ICM in galaxy clusters up to $z \approx 1.0$ has been discovered (Matsumoto et al. 2000), but even subtle hints of changes with redshift could have a profound impact on the general understanding of the processes involved in the ICM. This current study spatially resolves the temperature and metal (iron) abundance to higher redshifts than previous works, as well as determines whether there exists evidence for changes in the temperature or iron abundance profile with redshift.

For higher redshift clusters, studies of the evolution of the radial temperature and metallicity profiles has been reported out to a redshift ~ 0.3 (Leccardi & Molendi 2008b,a), and here the work is extended out to ~ 0.9 . The goal is to search for evolutionary changes in the radial profiles. The results can be used to determine the relative significance of processes such as ram pressure stripping, Active Galactic Nucleus (AGN) activity, and galactic winds in clusters of galaxies. The end results can then be compared directly to simulations such as Domainko et al. (2006). Throughout this paper the concordance model of cosmology with $H_0 = 71 \text{ km s}^{-1} \text{ Mpc}^{-1}$

$\Lambda_0 = 0.73$ and $\Omega_{m,0}=0.27$ is assumed. All calculations of cosmic distances and times are based on Wright (2006).

2. The Data

All data in this study were taken from the *Chandra* and *XMM-Newton* public archives, and are listed in Tables 1 & 2. Most of these observations were chosen after being included in Bonamente et al. (2006), Tozzi et al. (2003) or Leccardi & Molendi (2008b). All clusters listed here that are not found in these studies were found by searching the *Chandra* & *XMM-Newton* archives for galaxy cluster observations. The resulting sample was chosen to cover a large range of redshift with reasonable uniformity. This allowed for the sample to be conveniently divided into subsets which will be compared to one another, building on previous work at lower redshifts (De Grandi et al. 2004). The redshifts and coordinates of these clusters were provided by the NASA/IPAC Extragalactic Database (NED), and the hydrogen column densities are given by the n_H calculator provided on the HEASARC website. Investigations into the element abundances of galaxy clusters suggest that most of the elemental emission is dominated by iron, and that many other elements have abundance levels that do not change much with redshift (Baumgartner et al. 2005). This allowed for the use of iron abundance and metal abundance interchangeably, and although the model used in this work fit the abundance of all metals, the results of these fits will hereafter be called the iron abundance measurements.

2.1. Chandra Data Processing

All *Chandra* observations used herein were observed with the ACIS camera. All processing of *Chandra* data was carried out using CIAO 3.3 and all the contained packages including Sherpa and ChIPS and followed the general procedure found in Tozzi et al. (2003). For each data set the standard issue EVENTS LEVEL 1 file was reset to remove all corrections already implemented on the data set. The process *acisrunbadpix* was run on the reset file to detect all bad pixels. Next, the standard Level 1 events processing, *acisprocessevents*, was run on the reset file to create a new EVENTS LEVEL 1 file. Detection of very faint pixels was done whenever the data itself was taken in VFaint mode. The new Level 1 file was then filtered to only include the standard event grades 0,2,3,4, and 6 and also filtered further with the pipeline good time intervals to create a new EVENTS LEVEL 2 file. The new Level 2 file was processed further using the *destreak* routine and then using the *analyzeltcrv* routine as part of the ChIPS package to determine in greater detail the good time intervals. The bin time used for all data sets was 200 seconds. The de-streaked file was then filtered again using these good time intervals. As a final step in processing, the image was then filtered only to include the energy range of 0.3-10 keV. Filtering on the energy improves the signal to noise ratio of the image. The resulting event list was then used in all subsequent imaging and spectral analysis. There are 25 clusters observed using 27 *Chandra* observations, with redshifts ranging from 0.142 to 0.890. All of the cluster data sets, along with their Equatorial coordinates, redshifts, galactic hydrogen column densities, and

net exposure times after all processing are listed in Table 1.

2.2. XMM-Newton Data Processing

All *XMM-Newton* data analyzed in this project used all three EPIC cameras: MOS1, MOS2, and the PN camera. The software used was SAS version 7.0, the standard *XMM-Newton* processing software. All data sets were processed using the *images* script available on the *XMM-Newton* website. The *images* script first runs the fundamental SAS algorithms *cifbuild*, *odfingest*, *epchain*, and *emchain*. It then processes the standard event list further to improve signal-to-noise. In order to minimize the significance of flare events, the *images* script allows for the user to input desired Good-Time-Interval (GTI) for each data set. In this case the GTI intervals were chosen as time windows where the rate was less than 35 counts per 100 seconds for the MOS cameras, and 40 counts per 100 seconds for the PN camera. After GTI filtering the *images* script then cleans for bad pixels based on a separate input script, with default bad pixels provided by the *XMM-Newton* data center. The standard bad pixel table provided by the *images* script was used here. Although the *images* script was originally designed to create high quality images from all three cameras, the resulting event lists are still useful for spectral studies. Unlike the case of the *Chandra* data sets, the event lists used for *XMM-Newton* analysis have not been subject to any energy filtering before determining radial profiles. However, all spectra for both instruments are restricted to the energy range from 0.5-8.0 keV. As a final restriction, the PATTERNS on the events were limited to single, double, triple, and quadruple events for the MOS cameras (*PATTERN* ≤ 12) and limited to single and double events for the PN camera (*PATTERN* ≤ 4). Eight *XMM-Newton* data sets were considered in this study. They are listed along with Equatorial coordinates, redshifts, hydrogen column density, and net exposure times after all processing in Table 2.

2.3. Scale Lengths: The Core and Counts Radius

In order to average clusters together in a meaningful way, a scale length was needed. Two scale lengths were calculated for each cluster and used to divide the cluster into four annular regions: the first scale length was calculated by fitting the net intensity to a one-dimensional beta fit and the second by dividing the cluster into four regions with roughly equal numbers of net counts. The outer radii in these regions are labeled r_1 , r_2 , r_3 , and r_4 in Table 3. These radial profiles were determined using either the surface brightness (core) or the net counts (counts), and the background region for these calculations was always an annular region at least 5'' wide. This annular region was usually sufficiently small to minimize contamination from line-of-sight point sources while also containing enough counts ($\approx 100-1000$) to be statistically significant ($\sim 3-10\%$). In some cases, the background region needed to be larger to reach this level of significance, but a region with a significant number of counts (≥ 100) was always used. The profiles are not strongly sensitive to the number of counts used in the background regions, which were chosen specifically to be radially symmetric.

Table 1. Basic information about *Chandra* data sets used in this study.

Cluster Name	Obs #	Clusters analyzed from <i>Chandra</i>					Exposure Time (s)
		RA	DEC	z	$n_{\text{H}}(10^{22}\text{cm}^{-2})$		
Abell 1413	1661	11 55 18.20	+23 24 28.80	0.142	0.0219	9749	
Abell 2204	499	16 32 47.00	+05 34 33.00	0.152	0.0567	11250	
Abell 665	3586	08 30 45.20	+65 52 55.00	0.182	0.0431	28600	
RX J0439.0+0520	527	04 39 02.20	+05 20 43.00	0.208	0.1070	10830	
Abell 773	533	09 17 59.40	+51 42 23.00	0.217	0.0126	10500	
Abell 697	4217	08 42 53.30	+36 20 12.00	0.282	0.0341	18880	
Abell 611	3194	08 00 56.90	+36 03 26.00	0.288	0.0499	35990	
MS 1008.1-1224	926	10 10 32.33	+12 39 32.18	0.306	0.0726	42960	
MS 2137.3-2353	928	21 40 12.70	-23 39 27.00	0.313	0.0355	31990	
Abell 1995	906	14 52 50.40	+58 02 48.00	0.319	0.0145	43830	
ZWCL 1358+6245	516	13 59 50.60	+62 31 04.00	0.328	0.0193	45420	
MACS J2228.5+2036	3285	22 28 34.40	+20 36 47.00	0.412	0.0429	19700	
MACS J2214.9-1359	3259	22 14 57.30	-14 00 14.00	0.483	0.0328	17020	
MACS J1311.0-0310	3258	13 11 01.70	-03 10 41.00	0.490	0.0188	15000	
MS 0015.9+1609	520	00 18 33.86	+16 26 07.75	0.541	0.0407	66940	
MACS 1423.8+2404	4195	14 23 47.80	+24 04 41.40	0.545	0.0238	113400	
MS 0451.6-0305	529	04 54 10.90	-03 01 07.20	0.550	0.0500	16370	
MS 0451.6-0305	902	04 54 10.90	-03 01 07.20	0.550	0.0500	41470	
MACS J2129.4-0741	3199	21 29 26.20	-07 41 27.00	0.570	0.0484	17690	
MS 2053.7-0449	551	20 56 22.40	-04 37 43.00	0.583	0.0462	43100	
MS 2053.7-0449	1667	20 56 22.40	-04 37 43.00	0.583	0.0462	43900	
MACS J0647.7+7015	3196	06 47 50.20	+70 14 55.00	0.584	0.0563	18850	
CL 1120+4318	5771	11 20 07.60	+43 18 07.00	0.600	0.0208	19740	
MACS J0744.8+3927	3197	07 44 53.00	+39 27 26.00	0.686	0.0568	19690	
MS 1137.5+6625	536	11 40 23.30	+66 07 09.00	0.782	0.0121	119500	
RX J1716.9+6708	548	17 16 52.30	+67 08 31.20	0.813	0.0372	50350	
CL J1226.9+3332	3180	12 26 58.20	+33 32 48.00	0.890	0.0137	29470	

Table 2. Basic information about *XMM-Newton* data sets used in analysis.

Cluster Name	Obs #	Clusters Analyzed from <i>XMM-Newton</i>					Exposure Time (s)
		RA	DEC	z	$n_{\text{H}}(10^{22}\text{cm}^{-2})$		
Abell 1763	0084230901	13 35 17.20	+40 59 58.00	0.223	0.0082	19500/19500/9197	
Abell 2390	0111270101	21 53 34.60	+17 40 11.00	0.228	0.0619	13900/13900/9445	
Abell 1835	0147330201	14 01 02.00	+02 51 32.00	0.253	0.0204	78120/79450/32060	
RX J0256.5+0006	0056020301	02 56 29.51	+00 05 28.70	0.360	0.0650	19190/19170/7914	
RX J0318.2-0301	0056022201	03 18 28.76	-03 00 46.70	0.370	0.0505	20270/20340/11570	
RX J0426.1+1655	0056020401	04 26 04.20	+16 55 48.50	0.380	0.1910	18820/18820/8337	
RX J1120.1+4318	0107860201	11 20 00.91	+43 18 15.10	0.600	0.0203	22140/22150/16240	
CL J1226.9+3332	0200340101	12 26 58.00	+33 32 54.00	0.890	0.0138	77750/77780/60660	

Note: The exposure times for the *XMM-Newton* data sets are given in the following order: MOS1/MOS2/PN

For each cluster, both radii have been calculated using annular regions 2.''5 wide to determine the intensity profile across the cluster. Both scale radii were then used to determine regions for extracting spectra and measuring the average temperature and iron abundance profiles. The only profiles and measurements shown in the text will use the counts radius, the reasons for which will be discussed in §2.3.3. The measured core radius and counts regions are found in Table 3.

2.3.1. The Core Radius

The basis for using a core radius length scale is that cluster dynamics and the evolution of the ICM could be inter-related (e.g., Rosati et al. 2002), so a one-dimensional beta fit was performed on each cluster to determine the core radius scale. The centers were chosen by eye, and consistent with all attempts to determine the center of emission analytically. The error for choosing this center

was always a factor of 10 smaller than the calculated core radius. The radial profile of surface brightness was calculated using the the CIAO command *dmextract*, and the net counts annuli described in §2.3, and it was fit to the Sherpa *beta1d* model. The *beta1d* mode fits the data to a function of the form

$$I(x) = A \times \left[1 + \left(\frac{x - x_0}{r_c} \right)^2 \right]^{-3\beta+1/2} \quad (1)$$

where r_c is the core radius. The parameter β is a measure of the ratio of kinetic energy in the galaxies moving in the cluster to the thermal energy of the cluster (e.g., Rosati et al. 2002). The radial fits are described by the two parameters r_c and β . The offset from zero (x_0) was always fixed at zero, and the proportionality constant normalizes the fit to the particular data relating it to the central density of the cluster. Radial profiles are listed in Table 3, with the first eight observations being

from *XMM-Newton*. More elaborate fitting profiles like a double- β fit (Bonamente et al. 2006) could have been used in lieu of a single- β fit, but a single- β fit is usually all that statistics require (e.g., Ettori et al. 2004a). For clusters with high surface brightness in their center, however, a more appropriate fit may be the more elaborate model used by Kotov & Vikhlinin (2005).

2.3.2. The Counts Radius

Upon examination of the one-dimensional beta fits and their reduced χ^2 statistics, it appeared as though the beta model fits derived from Sherpa were not statistically robust. The reduced χ^2 for these fits was often above 2, and although others have used similar results (Sakelliou & Ponman 2004), it was judged necessary to find a second method used as to of independently verify the profiles. Therefore, a second set of temperature and iron profiles were calculated with the same set of data. The second method used was to divide the cluster into radial regions not by a constant length scale, but instead by giving each region a constant number of counts. The furthest extent of spectral extraction was also determined by the net counts in a $2.''5$ wide region. If the net counts next the $2.''5$ wide region out ever dropped below 20 for *Chandra* or 100 for *XMM-Newton* data, then this defined the edge of the cluster due to their low signal-to-noise ratio of the regions beyond this point. The four calculated counts regions for each cluster are listed in Table 3. Dividing the cluster in this manner also allows for all of the spectra for one cluster to be comparably significant instead of having a wide disparity in spectral quality. The spectra were extracted in exactly the same manner as the core radius spectra, which will be described in detail in §2.5. This process of sub-dividing the cluster will be called the counts profile or counts radius, hereafter. They will also be listed as r_1 , r_2 , r_3 , and r_4 as an abbreviation in the tables, particularly in Table 3

2.3.3. Differences Between the Two Profiles

The radial profiles in each cluster are compared in two ways in Tables 3 & 4. Table 3 shows the extents of each individual counts region as well as the calculated core radius and virial radius r_{200} in arcseconds. Table 4 shows the average core and counts regions in terms of kpc. It was found that there were insignificant differences between the two radii on average, except for the very outer region. The outermost counts regions are usually much wider than $2r_c$ (see the averages given in Table 4). Therefore, the average temperature and iron abundance measurements should be strongly correlated between the core and counts radius, with differences only being expected in the outermost regions. Also included in Table 3 is the calculated virial radius in arc seconds. The virial radius is calculated as found in Jones et al. (2003), divided by 1.4 to take into account the difference between cosmologies ($H_0 = 50 \text{ km s}^{-1} \text{ Mpc}^{-1}$ in Jones et al. (2003) while $H_0 = 71 \text{ km s}^{-1} \text{ Mpc}^{-1}$ here). The formula itself is given as

$$r_{200} = 2.779 \times \left(\frac{T}{10 \text{ keV}} \right)^{0.5} \times (1+z)^{-1.5} h_{71}^{-1} \text{ Mpc} \quad (2)$$

and the temperature used was the overall temperature measured by the procedure described in § 2.5. This allows for a direct comparison with other work that uses the virial radius. Typically a counts region bin corresponds to about $0.1 r_{\text{virial}}$, thus the profiles discussed here extend out on average to about $0.4 r_{\text{virial}}$. Although the core and counts radius were both used as scale radii for temperature and iron abundance profiles, the measurements for the core radius profile have been omitted from this text. The core radius results have been omitted because of their weaker statistics as well as the presence of two very small core radius measurements, noted in Table 4. The one-dimensional β -fit also suffers from bias in the presence of cool core clusters with high densities in the center. The radial profiles produced by the two different methods are very strongly correlated, and therefore the calculated results were not sensitive to this choice. Using the counts radius allows for more robust statistics and systematics.

Table 4. Average outer extent of the core and counts radius regions in kpc.

Radius	Outer extent of region in kpc			
	Region #1	Region #2	Region #3	Region #4
Core	87	173	260	347
Counts	84	177	314	607

2.4. Excluded Data

Each cluster had to satisfy two general conditions before included in this study. Each cluster first needed to have a sufficient number of counts to measure a temperature that was significantly ($> 2\sigma$) above zero. All of the clusters in this sample have more than an average of 1,000 counts per detector (3,000 for *XMM-Newton* observations, 1,000 for *Chandra* observations) within two core radii, and the minimum luminosity of all clusters from zero to two core radii is $1 \times 10^{44} \text{ erg s}^{-1}$. The second condition was morphological in nature, as it was necessary to have a reasonable β -fit to the data. Any observations that showed obvious visual signs of recent large merger activity were immediately excluded. Beyond that, several sets were excluded based on the values derived from the β -fit. In these cases the best fit core radius was larger than the furthest extent of the radial profile. These sets often had β values that were unrealistically large as well, usually well above $\beta = 2$. Since the fit was unreliable in both parameters, these clusters were not considered in this sample. Table 6 lists all the observations investigated, but not included, in this study and why they were not considered.

2.4.1. The Unusual Case of RX J1347.5-1145

The very luminous cluster RX J1347.5-1145 was also investigated using two observations: *Chandra* observation #3592 (Allen et al. 2002) and *XMM-Newton* observation #0112960101 (Gitti & Schindler 2005). Although it was sufficiently luminous and symmetric to be included here; the temperatures measured between these two observations did not agree within 3σ . After this work began, Ota et al. (2008) found a hot bubble in the southeast re-

Table 3. Radial profile parameters for all clusters. The *XMM-Newton* clusters are listed first.

Radial Profile Parameters*									
Cluster Name	RA (Center)	DEC (Center)	β	Core Radius	r_1	r_2	r_3	r_4	r_{200}
Abell 1763	13:35:18	+40 : 59 : 59	0.95 ± 0.03	$77.6^{+2.4}_{-2.6}$	32.5	22.5	30	37.5	717.0
Abell 2390	21:53:37	+17 : 41 : 40	0.572 ± 0.004	23.4 ± 0.4	22.5	22.5	30	70	729.1
Abell 1835	14:01:02	+02 : 52 : 40	0.635 ± 0.002	18.88 ± 0.1	12.5	12.5	17.5	57.5	549.8
RX J0256.5+0006	02:56:34	+00 : 06 : 25	$0.74^{+0.30}_{-0.01}$	$42.7^{+20.1}_{-0.7}$	22.5	15	17.5	20	249.3
RX J0318.2-0301	03:18:34	-03 : 02 : 59	$0.81^{+0.30}_{-0.02}$	$42.3^{+17.5}_{-1.3}$	20	15	17.5	22.5	253.8
RXJ0426.1+1655	04:26:08	+16 : 55 : 14	0.61 ± 0.02	15.9 ± 1.3	12.5	7.5	10	25	234.9
RXJ1120.1+4318	11:20:08	+43 : 18 : 05	0.93 ± 0.07	40.2 ± 2.9	17.5	10	15	20	149.2
CL J1226.9+3332	12:26:58	+33 : 32 : 45	0.85 ± 0.03	23.6 ± 0.9	12.5	7.5	10	22.5	146.8
Abell 1413	11:55:18	+23 : 24 : 13	0.85 ± 0.05	45.3 ± 3.3	25	17.5	25	57.5	764.4
Abell 2204 [†]	16:32:47	+05 : 34 : 27	0.551 ± 0.003	7.5 ± 0.2	10	12.5	22.5	80	558.4
Abell 665	08:30:59	+65 : 50 : 12	0.63 ± 0.02	36.6 ± 2.2	27.5	20	25	50	893.3
RX J0439.0+0520	04:39:02	+05 : 20 : 46	0.58 ± 0.02	10.3 ± 1.4	10	12.5	20	50	369.4
Abell 773	09:17:53	+51 : 43 : 47	1.51 ± 0.25	93.2 ± 11.3	27.5	15	20	45	743.7
Abell 611	08:00:56	+36 : 03 : 27	0.85 ± 0.04	28.8 ± 1.4	15	12.5	17.5	55	360.5
Abell 697	08:42:53	+36 : 20 : 12	0.98 ± 0.06	67.6 ± 3.8	30	20	25	67.5	448.1
MS 1008.1-1224	10:10:33	-12 : 39 : 59	0.69 ± 0.04	38.9 ± 3.6	25	20	25	55	328.2
MS 2137.3-2353	21:40:16	-23 : 39 : 43	0.70 ± 0.01	9.8 ± 0.3	7.5	7.5	15	70	270.5
Abell 1995	14:52:50	+58 : 02 : 48	1.43 ± 0.15	69.1 ± 5.5	25	15	20	50	382.0
ZWCL 1358+6245	13:59:51	+62 : 31 : 04	0.57 ± 0.01	13.4 ± 0.8	12.5	15	20	42.5	289.5
MACS J2228.5+2036	22:28:34	+20 : 37 : 23	1.47 ± 0.29	50.5 ± 7.1	15	10	12.5	27.5	278.5
MACS J2214.9-1359	22:14:58	-14 : 00 : 15	1.00 ± 0.13	36.6 ± 5.1	15	12.5	17.5	35	244.2
MACS J1311.0-0310	13:11:01	-03 : 10 : 31	1.13 ± 0.20	23.7 ± 4.4	10	10	10	37.5	201.7
MS 0015.9+1609	00:18:33	+16 : 26 : 07	1.08 ± 0.09	54.2 ± 4.0	22.5	15	20	57.5	221.0
MACS 1423.8+2404 [†]	14:23:49	+24 : 04 : 35	0.62 ± 0.01	6.6 ± 0.3	5	7.5	17.5	47.5	162.5
MS 0451.6-0305(#529)	04:54:12	-03 : 00 : 58	1.18 ± 0.19	51.7 ± 7.5	17.5	12.5	15	30	208.2
MS 0451.6-0305(#902)	04:54:11	-03 : 00 : 48	0.83 ± 0.03	36.1 ± 1.5	20	15	20	60	224.6
MACS J2129.4-0741	21:29:27	-07 : 41 : 26	0.66 ± 0.04	18.6 ± 2.2	12.5	10	15	37.5	185.2
MS 2053.7-0449(both)	20:56:22	-04 : 37 : 47	0.66 ± 0.05	18.2 ± 2.1	12.5	10	12.5	32.5	208.6
MACS J0647.7+7015	06:47:50	+70 : 14 : 55	0.91 ± 0.08	29.8 ± 3.1	15	10	15	37.5	233.8
RX J1120.1+4318	11:20:06	+43 : 18 : 06	1.17 ± 0.31	42.0 ± 9.7	15	10	12.5	22.5	141.3
MACS J0744.8+3927 [†]	07:44:52	+39 : 27 : 29	0.56 ± 0.03	8.0 ± 1.4	7.5	7.5	12.5	35	143.0
MS 1137.5+6625	11:40:23	+66 : 08 : 20	0.86 ± 0.07	18.8 ± 2.0	10	7.5	10	27.5	133.1
RX J1716.9+6708	17:16:49	+67 : 08 : 27	0.89 ± 0.19	24.4 ± 5.8	12.5	10	12.5	37.5	124.4
CL J1226.9+3332	12:26:58	+33 : 32 : 48	1.29 ± 0.30	27.6 ± 5.5	10	7.5	10	27.5	141.8

*All measurements of radial regions are given in arcseconds. [†] Denotes the two clusters with extremely small core radii. See §2.3.3**Table 5.** Observations investigated and not included in this study, along with the reasons they were excluded.

Clusters Not Analyzed			
Cluster Name	Observatory	Observation ID #	Reason for Exclusion
Abell 2163	<i>Chandra</i>	1653	Bad β -fit
Abell 2218	<i>Chandra</i>	1454	Bad β -fit
RX J122+4918	<i>Chandra</i>	1661	Bad β -fit
MACS J1149.5+2223	<i>Chandra</i>	1656	Bad β -fit
Abell 68	<i>Chandra</i>	3250	Bad β -fit
RCS J0439-2904	<i>Chandra</i>	3577	Not enough counts
Abell 370	<i>Chandra</i>	515	Bad β -fit
RX J1347.5-1145	<i>Chandra</i>	3592	See Section 2.4.1
RX J1200.8-0328	<i>XMM-Newton</i>	0056020701	Not enough counts
WARP J0152.7-1357	<i>XMM-Newton</i>	0109540101	Merger
RX J1334.3+5030	<i>XMM-Newton</i>	0111160101	Merger
Sharc-2	<i>XMM-Newton</i>	0111160201	Not enough counts
RX J1354.3-0222	<i>XMM-Newton</i>	0112250101	Not enough counts
RX J1347.5-1145	<i>XMM-Newton</i>	0112960101	See Section 2.4.1
MS 1208.71+3928	<i>XMM-Newton</i>	0112190201	Not enough counts

gion of this cluster. Thus, it was judged that this cluster is not relaxed enough to be considered in this study and was also excluded.

2.5. The Spectra

Spectra for each data set were extracted with routines in CIAO for *Chandra* or SAS for *XMM-Newton*. If the data set was from *Chandra* then the spectra were extracted using the *specextract* routine. If the data set was from *XMM-Newton*, then the OGIP Spectral Products routine found in the Graphical Interface of SAS after running *XMMSelect* was used. Spectra were taken of all four an-

nular regions in both scale lengths. When determining the average cluster temperature and iron abundance a circular region from $0 - 2r_c$ region was used. Background regions were always circles with radii comparable or larger than two core radii outside of the detectable emission and always on the same chip as the cluster image. The background regions remained consistent within each data set. These background regions are specifically chosen to contain as many counts as possible without including sources. Since radial symmetry is not a major concern with the spectral background, while the total number of counts is, this region is not the same background region used to determine the radial profiles. The software used to do

the spectral fitting was XSPEC 12.4.0, and the MEKAL model in XSPEC was always used along with the TBABS galactic absorption model. Since the spectra often had low numbers of counts, the modified Cash statistic was always used to determine the best-fit temperature and iron abundance simultaneously. The modified Cash statistic is ideal for fitting spectra with a low number of counts in each bin (Nousek & Shue 1989) and also allows for the use of a local background spectrum instead of fitting the background to a model. The only remaining free parameter in the fit was the normalization. The other parameters of the model were fixed: the redshifts were frozen at the values given by the NASA/IPAC Extragalactic Database (NED) while the hydrogen column densities were frozen to the values given by the n_H calculator on the HEASARC website. The solar abundance values used were those from Anders & Grevesse (1989). For the *XMM-Newton* spectra, all three instruments were fit simultaneously to the same spectral model to ensure the best use of the available statistics. The measured temperature and iron abundance profiles for each cluster are found in Table 6. For the four clusters in this study with multiple observations, the temperature and iron abundance were determined by fitting all of the observations simultaneously.

3. Selection Effects

In any population study, it is important to take into account selection effects within the sample itself. Two selection effects are important in this study: overall temperature and cooling time. These selection effects combined with the separation by redshift lead to eight different subsets of the sample which were then compared to one another. In Table 7, 8 subsets defined by their temperatures and cooling time are listed along with the number of clusters in each subset.

3.1. Temperature and Luminosity

The average temperature of this sample of clusters follows a trend that needs to be taken into consideration. There is an inherent expectation that clusters at higher redshift should exhibit higher temperatures due to the $L_x - T$ relationship (e.g., Ota et al. 2006; Pacaud et al. 2007; Ettori et al. 2002, and references therein). This is because more distant (higher redshift) clusters need to be more intrinsically luminous to be detected than low luminosity clusters. The X-ray bolometric luminosity is proportional to temperature as $L_{x,bol} \propto T^{2.5}$ (e.g., Ota et al. 2006). Thus on average, the observed clusters at higher redshift should tend to higher average temperatures. It was necessary to take into account this selection effect when searching for variations with redshift. Based on the available sample, the boundary between high and low temperature clusters was set to 6.8 keV. Setting the boundary to this temperature allows for comparably sized subsets for high and low temperature clusters, even after the two other selection effects (cooling time and redshift) are taken into account. The average radial profiles presented below are not strongly dependent on small changes (≈ 0.2 keV) to this boundary.

3.2. Central Cooling

An important mechanism in galaxy cluster evolution is the process of radiative cooling. The cooling time for a cluster can be well approximated by Sarazin (1988) as

$$t_{cool} = 8.5 \times 10^{10} \text{ yr} \left(\frac{n_p}{10^{-3}} \right)^{-1} \left(\frac{T_g}{10^8 \text{ K}} \right)^{1/2} \quad (3)$$

where n_p is the particle density in units of cm^{-3} and T_g is the temperature of the gas in Kelvin. By relating the measured temperature and luminosity to the density and performing the calculation, the cooling times for each of these clusters can be calculated. Because high densities reduce the radiative cooling time, radiative cooling is potentially significant only in the central regions of a cluster. Therefore, all cooling calculations used the temperature and luminosity measured for the innermost regions. The cooling times were calculated assuming that the density is constant within the region of zero to one-half of a core radius and that all of these clusters originally formed at a redshift of $z = 2$. For the calculation of the density, the bolometric luminosity (from 0–100 keV) and the volume of the 0– $0.5r_c$ region were used to determine an emissivity for the region, which can then be related to the density by Sarazin (1988) as

$$e^{ff} = \left(1.435 \times 10^{-27} \right) T_g^{1/2} n_p^2 \text{ erg cm}^{-3} \text{ s}^{-1} \quad (4)$$

This assumes that the X-ray emission is all due to thermal bremsstrahlung and also that the density and temperature of the ICM is constant within $0.5r_c$. A single beta fit was used instead of a more elaborate fit, and de-projection of hydrostatic equilibrium models was not done, as was carried by Bonamente et al. (2006). The cooling time only goes as the square root of the temperature, and hence it can be seen that any contamination of the temperature determination by the outer portions of the cluster (in cooling clusters only) would be a weak effect. In comparison with the cooling times calculated in Bonamente et al. (2006), there is only one discrepancy between their results and those derived here. The cluster MACS J2129.4-0741 has a cooling time slightly smaller than its age (4.64 Gyr as compared to 4.82 Gyr). Since this difference is small compared to the cooling time, and it is not listed as a cooling core cluster in Bonamente et al. (2006), it is treated in this study as a non-cooling core cluster as well.

The results of these calculations are listed in Table 8. The presence of cooling core clusters leads directly to another important process: central Active Galactic Nucleus (AGN) activity. For nearby clusters with cooling cores, it has been shown that they do not cool as quickly as the theoretical cooling times suggest (Fabian 1994). AGN activity could influence the temperature as far out as ≈ 50 – 100 kpc, which is, on average, approximately $0.5r_c$ or in the first counts profile bin. The majority of cool core clusters exhibit the radio emission or bubbles usually associated with AGN activity (Dunn & Fabian 2006). The findings of Dunn & Fabian (2006) also show that only a small fraction of cool core clusters show no evidence of AGN activity as either bubbles or radio sources. Therefore, it is expected that central AGN activity is generally (if not always) present in the cooling core clusters in this sample as well. For completeness, all clusters were searched for

possible counterpart radio sources within one arc-minute of the cluster position. The presence of sources was done using the NVSS catalog (Condon et al. 1998), and the sources were confirmed as being associated with the cluster using NED. The clusters with likely radio counterparts are denoted with a dagger in Table 8. The presence of central AGN activity will be assumed in discussing the results for cool core clusters.

4. Results

After dividing the sample into eight comparable subsets based on temperature, cooling time, and redshift, relevant average profiles were calculated and compared. These divisions had to be made so as to make valid comparisons between profiles derived from low and high redshifts. Since there is currently little evidence for evolution in galaxy clusters even at high redshifts (Matsumoto et al. 2000; Mushotzky & Loewenstein 1997), the null hypothesis for statistical tests will be that cluster abundance and temperature profiles do not change with redshift. See also Leccardi & Molendi (2008a,b) for $z = 0.1-0.3$ studies. Only if the statistics conclusively suggest rejecting this hypothesis will evolution be considered.

4.1. Zero iron abundances and N/A values

As seen in Table 6, there are several instances where the best fit iron abundance was zero. As a compromise between ignoring these points altogether and producing an un-weighted average, the derived uncertainties to these points were used as statistical weights (one over the error squared). Since these zero values were most likely due to an insufficient number of detected photons rather than a true lack of iron in the ICM, this averaging was judged to be a valid approach. As a cross check, these points were excluded from the averaging as well, and the results were all within 1σ of each other in both weighted and unweighted averages (see §4.2). Also, there was one instance where the measurement failed to converge for both the temperature and iron abundance simultaneously, and no measurement errors could be calculated. This measurement is listed with a “N/A” in Table 6.

4.2. Averaging Procedures

In order to make the most robust study of the data, two averaging procedures (weighted and unweighted) were done on each subset listed in the following sections. The primary averaging process used was a weighted average that took into account the measurement error on each observation. For a given sample of N clusters, the weighted temperature/iron abundance average \bar{M} is calculated using the measurements m_i and the measurement error σ_i as

$$\bar{M} = \frac{\sum_{i=1}^N \frac{m_i}{\sigma_i^2}}{\sum_{i=1}^N \frac{1}{\sigma_i^2}} \pm \left(\sum_{i=1}^N \frac{1}{\sigma_i^2} \right)^{-1/2} \quad (5)$$

As a check to ensure that no significant biases arise due to the weighting procedure, a standard (unweighted) mean and standard deviation on that mean were also calculated, both of which only depend on the measurements

themselves and not the error on those measurements. The unweighted averages further demonstrate the robustness of these measurements, as the choice of weighted or un-weighted averaging does not affect the basic conclusions.

4.3. Average Profiles

The average temperature and iron abundance profiles are written out in Tables 9 & 10. They are organized by subset and radial region, and show the unweighted values in parentheses next to the weighted averages. Since the weighted mean emphasizes measurements with the smallest errors and there was substantial variance in the quality of the spectra, the weighted mean was chosen to be the basis for the subsequent figures and discussion. However, both means exhibited the same general trends and results.

4.4. Temperature Profiles

The temperature profiles of Table 9 suggest that the overall temperature and cooling time completely define the temperature profiles of clusters. The average temperature profiles for cooling core clusters exhibit a clear increase in temperature with radius, while clusters without cool cores are either isothermal or have temperatures that decrease with radius. Similar temperature profiles for non-cool core clusters has been confirmed by Sanderson et al. (2006) & Leccardi & Molendi (2008b).

There are also no differences between the temperature profiles of high and low temperature clusters of comparable cooling times with the exception of an overall offset due to the higher overall temperatures. Because the temperature profiles do not seem to deviate from expectations based on their overall temperature and cooling times, the discussion in §5 will focus primarily on the measured iron abundance profiles.

4.5. Iron Profiles

The iron abundance radial profiles are now taken into consideration.

4.5.1. Low Temperature, Cool Core Clusters

The first subsets to consider are those of low temperature, cool core clusters. These clusters have been shown to have strong iron abundance gradients (De Grandi et al. 2004) at low redshifts and are often associated with central AGN activity. Not only do the two subsets considered here (subsets # 1 & 5) show no evidence for evolution with redshift, the iron abundance profile is almost identical to the profiles of still lower ($z \leq 0.1$) redshift clusters discussed in De Grandi et al. (2004). The results of De Grandi et al. (2004) have been re-projected to the length scale used here and corrected for the differences in their solar abundance model. All three profiles are shown in Fig. 1. From Fig. 1 there is no evidence for evolution in the iron abundance of cool core clusters from $\langle z \rangle \approx 0.7$ to $\langle z \rangle \approx 0$. It should also be noted in Table 10 that low temperature cool core clusters (subsets 1 & 5) do not have statistically significant differences in overall iron abundance or in average iron abundance profiles versus redshift. The same lack of difference is also seen when

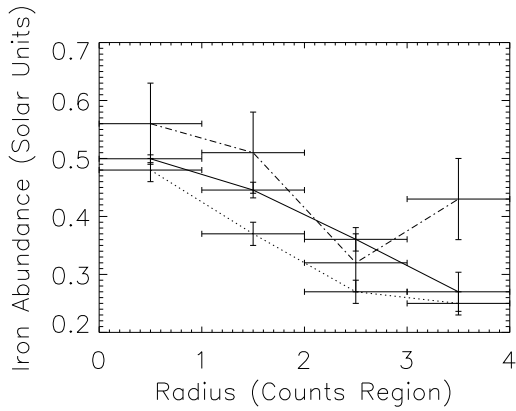


Fig. 1. Iron abundance as a function of radius for clusters with low temperatures and short cooling times, separated by redshift. The dotted line corresponds to subset # 1 ($z < 0.4$) while the dashed line corresponds to subset # 5 ($z > 0.4$). The solid line is from De Grandi et al. (2004).

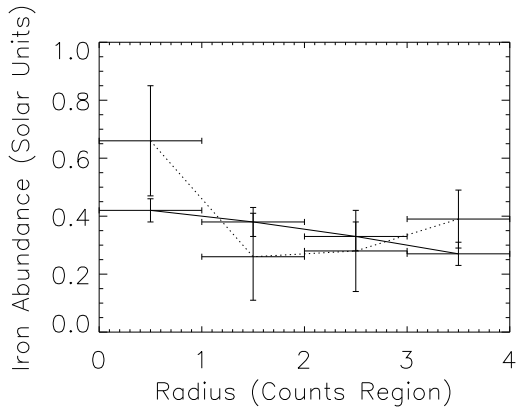


Fig. 2. Iron abundance as a function of radius for clusters with high temperatures and short cooling times, separated by redshift. The solid line corresponds to subset # 2 ($z < 0.4$). The dashed line corresponds to subset # 6 ($z > 0.4$).

comparing high temperature cool core clusters (subsets 2 & 6).

4.5.2. High Temperature, Cool Core Clusters

There are only two clusters in the high redshift subset for clusters with high temperatures and cool cores (subset # 6) which is too small of a sample to be considered representative of the entire population. However, it should nevertheless be noted that the average iron abundance profile for this small subset is entirely consistent point-for-point with the results of the larger low redshift sample. As can be seen in Figure 2, the average profile in both cases has a higher central abundance, with evidence for a decreasing gradient outward. Even though the average profile for the high redshift sample may not represent the population, this small sample still shows no evidence for evolution in the iron abundance profile with redshift.

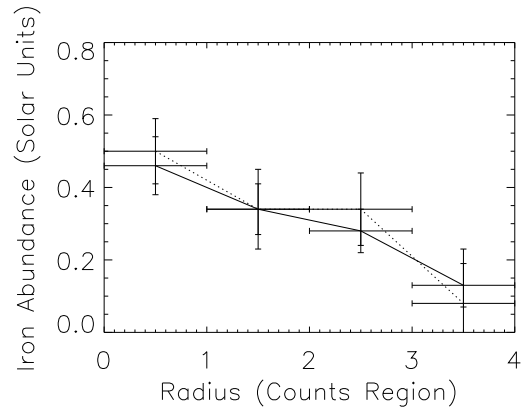


Fig. 3. Iron abundance as a function of radius for clusters with low temperatures and long cooling times, separated by redshift. The solid line corresponds to subset # 3 ($z < 0.4$). The dashed line corresponds to subset # 7 ($z > 0.4$).

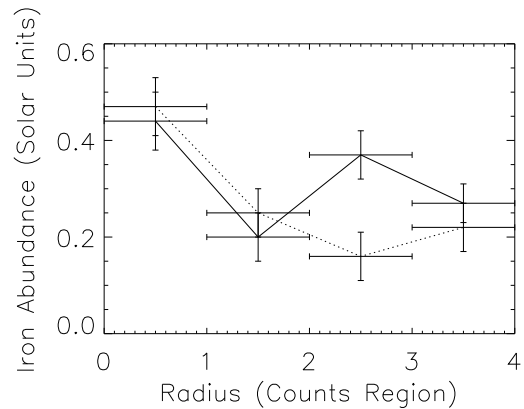


Fig. 4. Iron abundance as a function of radius for high temperature clusters with long cooling times, separated by redshift. The solid line corresponds to subset # 4 ($z < 0.4$). The dashed line corresponds to subset # 8 ($z > 0.4$).

4.5.3. Low Temperature, Non-Cool Core Clusters

Subsets # 3 & 7 describe the average profiles for low temperature clusters without cool cores. Although both of these samples are small, Figure 3 shows that the two profiles are very consistent with one another.

4.5.4. High Temperature, Non-Cool Core Clusters

Both subsets in this case have a relatively high number of clusters. Again in these two subsets, the two radial profiles are wholly consistent with one another, with no reason to believe that the iron abundance in these subsets is changing with redshift. All of the analysis suggests that the iron abundance is not evolving with redshift independent of the temperature and cooling time.

5. Discussion

5.1. The Data Analysis

Before discussing the radial dependencies of the iron abundance and the temperature, it is worthwhile to review

why and how the data from the clusters were averaged together in the manner that was done. As noted in § 2.3 and 2.4, two different radii/scales were chosen. The first was the core radius derived from a single β model. This radius corresponds directly to the dynamical scale of the cluster. This is the natural choice for a scale length here, as it is based on the dynamics of the cluster.

A second scale length was used to find four radial regions with approximately equal numbers of net counts. Although this scale is independent of the dynamics, it is useful for testing whether the profiles are sensitive to the scale length chosen. This "equal counts per enclosed area" process was chosen for its simplicity in calculation, and for its ability to increase the significance of measurements in the outer regions of the clusters. When the counts and core radii were converted into a linear projected length scale such as Mpc, they cover very similar ranges. The main inconsistency occurs in the outermost regions, where the counts radius extends much further outward than the core radius. Therefore, overall consistency between the results derived by the two different methods was expected. Since the counts radius is so strongly correlated with the core radius and offers better statistics across each cluster, the results of the core radius measurements have been omitted from the text even though they are wholly consistent with these results.

Another possible choice of length scale is the virial radius of the cluster, but the easiest way of estimating r_{virial} (or r_{200}) relates directly to the overall temperature (e.g., Jones et al. 2003). If the virial radius was used in this case, the temperature would be correlated with the radial regions. Because of the $L_{\text{x,bol}} - T$ relationship (e.g. Ota et al. 2006) and clusters at higher redshifts must be on average more luminous to be detected with a sufficient statistical significance, the scale radius chosen needs to take into account this selection effect. Because the virial radius is related to the overall temperature, and therefore luminosity, it is difficult to correct for this selection effect. As an example, there exist nearby clusters such as Perseus (Arnaud et al. 1994) and Coma (e.g., Watanabe et al. 1999; De Grandi et al. 2004; Adami et al. 2006) with comparable X-ray luminosities that exhibit very different temperature and iron abundance profiles.

As a further check of our analysis, our results were compared with other published measurements such as Kotov & Vikhlinin (2005) for CL 0016+16 (MS 0015.9+1609), and the temperature/abundance results published here tend to be higher by $\sim 1 - 1.5\sigma$ than those of Kotov & Vikhlinin (2005). The work of Balestra et al. (2007) shows how using an updated analysis tool can bring out difference of this scale. Furthermore, the differences may be due to systematics between the *Chandra* and *XMM-Newton* analysis chains as well as the statistics between the two observations themselves. These differences in the core radius measurements are on the order of about 20% which should not strongly affect the results of the average profiles. The measured profiles of Kotov & Vikhlinin (2005) also measure the radial profile in a different energy band than our measurement (0.5-2 keV in Kotov & Vikhlinin (2005) versus 0.5-10 keV in this work). Three other clusters were studied by Snowden et al. (2008), and these results are consistent within 10-20% and usually within 1 standard deviation. An important caveat is that Snowden et al. (2008) used

the MOS cameras of *XMM-Newton*, whereas *Chandra* was used in this study for measuring the temperature of Abell 1413 and Abell 2204. The systematic differences in response and sensitivity may be responsible for the discrepancies between the results of Snowden et al. (2008) and those listed here.

The results of the counts profiles results will now be taken at face value, and the physical interpretation of noticeable variations will be discussed.

5.2. Review and Comparison With Previous Work on the Chemical Evolution of the ICM

Balestra et al. (2007), Maughan et al. (2008), and Werner et al. (2008) all discuss evidence for the chemical evolution of the ICM. Older works (e.g., Mushotzky & Loewenstein 1997; Rizza et al. 1998) did not report any statistically significant evidence for chemical evolution with redshift. The recent work that found the strongest evidence for evolution is Balestra et al., but this evolution was found only when data based on all the $z < 1$ clusters in their sample were combined (compare with the smaller previous set in their Fig. 3). Furthermore, the derived chemical evolution required the use of the formal statistical best fit uncertainty instead of the observed dispersions (e.g. their Fig. 14). In contrast, for a similar redshift range (below about 0.9), the results of Maughan et al. are consistent with no evolution.

From the theoretical point of view as described in Kapferer et al. (2007), Sarazin (1988), and references therein, the chemical evolution of the ICM is a complex combination of effects due to cluster merging, infall of enriched material, galactic ram pressure stripping, galactic winds, and other possible causes. For the relaxed clusters considered in this paper Kapferer et al. (2007) predicted no observable chemical evolution from redshift 0.15 to 0.9.

Our paper shows how it is important to compare like clusters and that there is room for further theoretical studies to understand the apparent lack of evolution of the radial dependence of the enriched material of the ICM, and at the same time induce heating via infall of metal rich gas clouds.

5.3. Scenarios for heating and iron enrichment

The data presented here are consistent with no evolution in radial profiles of iron abundance and temperature. The modeling of this should be consistent with the concept of hierarchical formation of structure in the universe (e.g. Gao et al. 2008, and references therein). Because the iron abundance does not appear to be strongly correlated to the overall temperature, gravitational infall is the most likely scenario for heating clusters beyond ≈ 6.5 keV. This infall must take place in such a manner as not to change the radial profile of iron abundance or temperatures. For non-cooling clusters this means the clusters somehow have no measurable temperature gradients inside about 500 kpc but maintain their abundance gradients while (presumably) increasing in temperature in a hierarchical growth model. In order to demonstrate why infall is the preferred major energy input, the process of heating has to be considered in some detail.

An estimate of the amount of near solar abundance material that is added along with the energy to boost the $\langle kT \rangle$ from 4 keV to 8 keV is made now. We assume typical $L_X - T$ (Ota et al. 2006; Ettori et al. 2004b; Stanek et al. 2006) and $L_X - M$ (e.g. Rykoff et al. 2008; Stanek et al. 2006) relations apply to the clusters studied here. Under these assumptions, if the temperature increases by a factor of 2 then the luminosity increases by at least a factor of 4 and the mass by a factor of 3, the amount of mass added to the clusters being on the order of $3 \times 10^{14} M_\odot$. Since galaxies are thought to make up only about 1/5 of the baryonic mass in clusters (see Loewenstein 2006, and references there in), it is implausible that this mass and additional gravitational energy is added by normal galaxies. This mass and gravitational energy must come instead from the infall of atypical galaxies that have gas masses that greatly exceed their stellar masses or gas clouds that never formed into galaxies. Damped Lyman α absorbers (DLAs) have metallicities that are near solar at z of 1 or higher (Meiring et al. 2007, and references therein) which makes the ability to add both mass and metals via infalling clouds plausible. It is beyond the scope of this work, though, to carry out detailed calculations of this infall scenario. However, an implication of the estimates made here is that sight lines on the outskirts of clusters should show the presence of DLAs at the cluster redshift. Furthermore, if mass is added with energy as implied by the $L - T$ and $L - M$ relationships used here, this rules out processes which might provide energy and metals but not significant amounts of additional mass, such as SN or AGNs.

Instead, suppose that the $L - M$ relationship used here doesn't apply to these high z clusters. In this case, supernovae would still not be a plausible explanation. This is because the energy input of approximately 10^{64} ergs would require an unreasonably high number of SNe when all the available energy is transferred to the ICM (Conroy & Ostriker 2008). For example, suppose there are 1,000 galaxies per cluster. This translates into 10^{10} SNe per galaxy or 10^1 SNe/year for 10^9 years. It is also implausible that a central AGN could provide this much heat (10^{64} ergs), as this heat would require 10^{55} erg/year deposited for 1 Gy, or 10^{47} erg s^{-1} minimum energy generation assuming 100% efficiency in transferring energy to heat. Since the magnitude of heating seems beyond what central AGN activity could provide an infall scenario is a more likely explanation.

5.4. Scenarios for Mixing

Since there is no evidence for evolution in every type of cluster considered in this study (as seen in the figures), it will be assumed for the sake of discussion that clusters are not mixing over this range of redshifts.

Beginning with the cool core clusters in Fig. 1, it is seen that they exhibit almost no signs of evolution in their iron abundance profiles from the 0.4-0.9 redshift bin up to the present day, even though there is a very clear gradient at all redshifts. This suggests two possible scenarios: either enrichment and mixing both exist in such a way that neither is dominant, or neither process occurs. If neither process occurs, the unchanging iron abundance profile can be explained as being due to the average cluster galaxy having lost most of its gas by $z \sim 0.8$. In

this case the galaxies have no gas to stir up and mix the ICM. An absence of gas in cluster galaxies would also manifest itself in a low, non-evolving star formation rate (Homeier et al. 2005). A low star formation rate occurs if ram pressure stripping has removed the majority of the gas from most of the cluster galaxies before redshift $z = 0.8$ within 500 kpc of the cluster center, well within the regions observed in this study. The suggestion that most gas is stripped from galaxies by $z \approx 0.4$ was also seen by Butcher & Oemler (1984); Dressler et al. (1997).

As the gradient in iron abundance has remained constant with redshift, there is also no evidence for growth in the gradient. Substantial changes in the abundance gradient would be expected if there was continuous activity from the central AGN. Therefore, energy input to the ICM beyond gravitational infall (Bode et al. 2007) must not have caused appreciable iron enrichment.

For non-cool core and high temperature clusters, there is less statistical evidence to suggest that the iron abundance decreases with radius in the same manner as low temperature cool-core clusters. However, as noted above, it is assumed there is no evolution in the radial profiles of the ICM with redshift. In this case, galactic motion within the cluster does not result in ram pressure stripping, one of the key processes for iron enrichment (and possibly mixing) in the ICM. Without ram pressure stripping from galaxies to enrich or mix the ICM, the iron abundance (and iron abundance profile) of the ICM remains static over long times.

6. Summary and Conclusions

Average radial profiles of the temperature and iron abundance of X-ray bright clusters in the redshift range from about 0.14 to 0.9 were calculated. We find no evidence for evolution within similar sets of clusters. The total element abundance remains constant with decreasing z and the gradients remain approximately the same. These observations suggest that gravitational infall is the dominant mechanism for heating of the ICM, and also that ram pressure stripping does not substantially change the ICM out to large redshifts. If clusters experience a significant (factor of 2 or more) amount of gravitational mass infall, then the iron abundance profile remains constant while the overall temperature increases. This infall needs to simultaneously keep the profile (within error of about 20%) isothermal while also maintaining the same iron abundance profile. Mass and energy considerations suggest infall of metal rich gas, but how the process takes place needs further theoretical study. These same considerations of mass and energy suggest that although central AGN activity is directly related to cooling cores, the central AGN does not produce significant amounts of metal rich gas and energy to the ICM beyond its local environment of about 50-100 kpc.

Other theoretical challenges to consider include how clusters formed in the first place with both abundance gradients and isothermal temperature profiles. Work also needs to be done on how the frequency and scale of merger activity (e.g. Wik et al. 2008) changes the abundance and temperature gradients of clusters. Another potentially important aspect of modeling galaxy clusters theoretically appears to be an accurate modeling of the local environment surrounding the cluster, as the infall of mate-

rial initially outside of the cluster could play an important role in its evolution.

From an observational point of view it will be interesting to measure temperature and abundance gradients for clusters at z greater than 0.9 as well as make measurements of DLAs by means of QSOs whose sight lines are at $\lesssim 1$ Mpc distances from the centers of rich clusters. These measurements may help determine more conclusively whether galaxy clusters are evolving in the ways described here and what kind of material might be falling in to cause the highest temperature clusters of galaxies.

Acknowledgements. This research has made use of the NASA/IPAC Extragalactic Database (NED) which is operated by the Jet Propulsion Laboratory, California Institute of Technology, under contract with the National Aeronautics and Space Administration.

We would like to thank the Max Planck Institut für Kernphysik in Heidelberg, Germany and Le Laboratoire d'Astrophysique de Marseille in Marseille, France for their hospitality. We would also like to thank A. Kathy Romer and Kivanc Sabirli for providing processed XMM data used in the early stages of this analysis. We would also like to thank Wilfried Domainko for his review and suggestions for improvement. We thank the referee for many insightful comments that greatly improved the manuscript. Finally, we would like to acknowledge support from NASA Illinois Space Grant NGT5-40073.

References

- Adami, C., Picat, J. P., Savine, C., et al. 2006, *A&A*, 451, 1159
- Allen, S. W., Schmidt, R. W., & Fabian, A. C. 2002, *MNRAS*, 335, 256
- Anders, E. & Grevesse, N. 1989, *Geochim. Cosmochim. Acta*, 53, 197
- Arnaud, K. A., Mushotzky, R. F., Ezawa, H., et al. 1994, *ApJ*, 436, L67
- Arnaud, M. 2005, in *Background Microwave Radiation and Intracluster Cosmology*, ed. F. Melchiorri & Y. Rephaeli, 77
- Balestra, I., Tozzi, P., Ettori, S., et al. 2007, *A&A*, 462, 429
- Baumgartner, W. H., Loewenstein, M., Horner, D. J., & Mushotzky, R. F. 2005, *ApJ*, 620, 680
- Bode, P., Ostriker, J. P., Weller, J., & Shaw, L. 2007, *ApJ*, 663, 139
- Bonamente, M., Joy, M. K., LaRoque, S. J., et al. 2006, *ApJ*, 647, 25
- Butcher, H. & Oemler, Jr., A. 1984, *ApJ*, 285, 426
- Condon, J. J., Cotton, W. D., Greisen, E. W., et al. 1998, *AJ*, 115, 1693
- Conroy, C. & Ostriker, J. P. 2008, *ApJ*, 681, 151
- De Grandi, S., Ettori, S., Longhetti, M., & Molendi, S. 2004, *A&A*, 419, 7
- Domainko, W., Mair, M., Kapferer, W., et al. 2006, *A&A*, 452, 795
- Dressler, A., Oemler, A. J., Couch, W. J., et al. 1997, *ApJ*, 490, 577
- Dunn, R. J. H. & Fabian, A. C. 2006, *MNRAS*, 373, 959
- Ettori, S., De Grandi, S., & Molendi, S. 2002, *A&A*, 391, 841
- Ettori, S., Tozzi, P., Borgani, S., & Rosati, P. 2004a, *A&A*, 417, 13
- Ettori, S., Tozzi, P., Borgani, S., & Rosati, P. 2004b, *A&A*, 417, 13
- Fabian, A. C. 1994, *ARA&A*, 32, 277
- Fabian, A. C., Sanders, J. S., Taylor, G. B., et al. 2006, *MNRAS*, 366, 417
- Gao, L., Navarro, J. F., Cole, S., et al. 2008, *MNRAS*, 387, 536
- Gitti, M. & Schindler, S. 2005, *Advances in Space Research*, 36, 613
- Homeier, N. L., Demarco, R., Rosati, P., et al. 2005, *ApJ*, 621, 651
- Jones, L. R., Ponman, T. J., Horton, A., et al. 2003, *MNRAS*, 343, 627
- Kapferer, W., Kronberger, T., Weratschnig, J., et al. 2007, *A&A*, 466, 813
- Kotov, O. & Vikhlinin, A. 2005, *ApJ*, 633, 781
- Leccardi, A. & Molendi, S. 2008a, *A&A*, 487, 461
- Leccardi, A. & Molendi, S. 2008b, *A&A*, 486, 359
- Loewenstein, M. 2006, *ApJ*, 648, 230
- Matsumoto, H., Tsuru, T. G., Fukazawa, Y., Hattori, M., & Davis, D. S. 2000, *PASJ*, 52, 153
- Maughan, B. J., Jones, C., Forman, W., & Van Speybroeck, L. 2008, *ApJS*, 174, 117
- Meiring, J. D., Lauroesch, J. T., Kulkarni, V. P., et al. 2007, *MNRAS*, 376, 557
- Mushotzky, R. F. & Loewenstein, M. 1997, *ApJ*, 481, L63
- Nousek, J. A. & Shue, D. R. 1989, *ApJ*, 342, 1207
- Ota, N., Kitayama, T., Masai, K., & Mitsuda, K. 2006, *ApJ*, 640, 673
- Ota, N., Murase, K., Kitayama, T., et al. 2008, *A&A*, 491, 363
- Pacaud, F., Pierre, M., Adami, C., et al. 2007, *MNRAS*, 382, 1289
- Rizza, E., Burns, J. O., Ledlow, M. J., et al. 1998, *MNRAS*, 301, 328
- Rosati, P., Borgani, S., & Norman, C. 2002, *ARA&A*, 40, 539
- Rykoff, E. S., Evrard, A. E., McKay, T. A., et al. 2008, *MNRAS*, 387, L28
- Sakelliou, I. & Ponman, T. J. 2004, *MNRAS*, 351, 1439
- Sanderson, A. J. R., Ponman, T. J., & O'Sullivan, E. 2006, *MNRAS*, 372, 1496
- Sarazin, C. L. 1988, *X-ray emission from clusters of galaxies* (Cambridge Astrophysics Series, Cambridge: Cambridge University Press)
- Snowden, S. L., Mushotzky, R. F., Kuntz, K. D., & Davis, D. S. 2008, *A&A*, 478, 615
- Stanek, R., Evrard, A. E., Böhringer, H., Schuecker, P., & Nord, B. 2006, *ApJ*, 648, 956
- Tozzi, P., Rosati, P., Ettori, S., et al. 2003, *ApJ*, 593, 705
- Watanabe, M., Yamashita, K., Furuzawa, A., et al. 1999, *ApJ*, 527, 80
- Werner, N., Durret, F., Ohashi, T., Schindler, S., & Wiersma, R. P. C. 2008, *Space Science Reviews*, 134, 337
- Wik, D. R., Sarazin, C. L., Ricker, P. M., & Randall, S. W. 2008, *ApJ*, 680, 17
- Wright, E. L. 2006, *PASP*, 118, 1711

Table 6. Temperature and iron abundance measurements for all clusters by counts region.

Temperatures and Iron Abundance Measurements									
Cluster Information		Temperatures in keV				Iron Abundances in Z_{\odot}			
Cluster Name	z	Region #1	Region #2	Region #3	Region #4	Region #1	Region #2	Region #3	Region #4
Abell 1413	0.142	6.0 ± 0.4	7.8 ± 0.7	7.4 ± 0.7	5.5 ± 0.4	0.46 ± 0.14	0.41 ± 0.16	0.49 ± 0.11	0.73 ± 0.14
Abell 2204	0.152	3.9 ± 0.1	6.7 ± 0.3	10.2 ± 0.7	12.1 ± 0.8	0.98 ± 0.09	0.57 ± 0.09	0.41 ± 0.11	0.25 ± 0.06
Abell 665	0.182	7.7 ± 0.7	7.9 ± 0.7	8.5 ± 0.7	8.1 ± 0.6	0.32 ± 0.12	0.39 ± 0.13	0.47 ± 0.14	0.31 ± 0.10
RX J0439.0+0520	0.208	3.1 ± 0.2	4.5 ± 0.3	4.8 ± 0.5	4.2 ± 0.5	0.50 ± 0.19	0.94 ± 0.28	0.44 ± 0.13	0 + 0.32
Abell 773	0.217	7.3 ± 1.0	9.1 ^{+1.9} _{-1.3}	9.6 ^{+1.8} _{-1.1}	8.1 ^{+1.3} _{-1.1}	0.43 ± 0.22	0.27 ± 0.23	0.68 ± 0.28	0.07 ^{+0.25} _{-0.07}
Abell 1763	0.223	7.5 ± 0.4	8.3 ± 0.4	7.0 ± 0.3	6.6 ± 0.3	0.47 ± 0.08	0.30 ± 0.08	0.30 ± 0.06	0.26 ± 0.05
Abell 2390	0.228	7.3 ± 0.2	9.4 ± 0.3	10.0 ± 0.5	9.7 ± 0.4	0.43 ± 0.05	0.43 ± 0.06	0.29 ± 0.06	0.17 ± 0.05
Abell 1835	0.253	5.0 ± 0.1	6.8 ± 0.1	7.2 ± 0.1	7.4 ± 0.1	0.46 ± 0.02	0.37 ± 0.02	0.26 ± 0.02	0.23 ± 0.02
Abell 697	0.282	9.4 ± 0.9	9.6 ± 1.0	9.3 ± 1.0	9.1 ± 1.0	0.50 ± 0.16	0.37 ± 0.15	0.54 ± 0.11	0.31 ± 0.09
Abell 611	0.288	6.7 ± 0.4	7.0 ± 0.5	7.5 ± 0.6	6.5 ± 0.5	0.45 ± 0.12	0.24 ± 0.10	0.21 ± 0.11	0.34 ± 0.07
MS 1008.1-1224	0.306	5.9 ± 0.5	5.8 ± 0.6	7.4 ± 0.8	6.5 ± 0.7	0.50 ± 0.14	0.35 ± 0.10	0.37 ± 0.10	0.04 ^{+0.10} _{-0.04}
MS 2137.3-2353	0.313	4.1 ± 0.1	5.1 ± 0.2	5.9 ± 0.3	5.8 ± 0.5	0.42 ± 0.06	0.32 ± 0.06	0.32 ± 0.07	0.35 ± 0.06
Abell 1995	0.319	8.3 ± 0.7	9.9 ± 0.8	8.6 ± 0.8	8.8 ± 1.0	0.33 ± 0.12	0.04 ^{+0.11} _{-0.04}	0.36 ± 0.10	0.36 ± 0.11
ZWCL 1358+6245	0.328	4.5 ± 0.2	8.9 ± 0.7	8.5 ± 1.2	9.4 ± 1.8	0.45 ± 0.10	0.42 ± 0.14	0.27 ± 0.18	0.69 ^{+0.10} _{-0.38}
RX J0256.5+0006	0.360	5.5 ± 0.4	5.4 ± 0.5	4.4 ± 0.4	3.7 ± 0.2	0.31 ± 0.13	0.39 ± 0.14	0.23 ± 0.10	0.38 ± 0.14
RX J0318.2-0301	0.370	4.0 ± 0.3	5.5 ± 0.5	5.3 ± 0.6	6.3 ± 0.8	0.55 ± 0.12	0.27 ± 0.14	0.21 ± 0.14	0.29 ± 0.17
RX J0426.1+1655	0.380	4.5 ± 0.4	6.4 ± 1.0	4.9 ± 0.7	5.0 ± 0.7	0.47 ± 0.15	0.06 ^{+0.18} _{-0.06}	0.07 ^{+0.16} _{-0.07}	0.38 ± 0.22
MACS J2228.5+2036	0.412	7.6 ± 1.3	9.9 ± 2.2	7.9 ± 1.4	6.9 ± 0.8	0.56 ± 0.21	0.26 ± 0.19	0.29 ± 0.15	0.52 ± 0.13
MACS J2214.9-1359	0.483	8.0 ± 1.2	9.1 ± 1.7	12.7 ^{+5.3} _{-2.8}	8.4 ± 1.5	0.27 ± 0.21	0.23 ± 0.22	0.17 ^{+0.20} _{-0.17}	0.13 ^{+0.18} _{-0.13}
MACS J1311.0-0310	0.490	4.7 ± 0.5	6.8 ± 0.9	7.4 ± 1.3	4.8 ± 0.6	0.19 ± 0.15	1.36 ^{+0.51} _{-0.23}	0.09 ^{+0.20} _{-0.09}	0.22 ± 0.17
MS 0015.9+1609	0.541	9.3 ± 0.8	9.9 ± 1.0	10.5 ^{+1.5} _{-0.7}	10.3 ± 1.1	0.61 ± 0.14	0.22 ± 0.08	0.09 ± 0.09	0.16 ± 0.09
MACS 1423.8+2404	0.545	4.1 ± 0.1	5.8 ± 0.2	7.1 ± 0.3	6.9 ± 0.5	0.66 ± 0.08	0.48 ± 0.07	0.34 ± 0.05	0.47 ± 0.07
MS 0451.6-0305	0.550	9.9 ± 0.8	8.9 ± 0.6	9.0 ± 0.7	7.3 ± 0.6	0.64 ± 0.14	0.28 ± 0.10	0.16 ± 0.10	0.49 ± 0.13
MACS J2129.4-0741	0.570	7.0 ± 1.1	7.2 ± 1.2	7.6 ± 1.2	5.2 ± 0.7	0.45 ± 0.24	0.33 ± 0.20	0.41 ± 0.23	0.65 ± 0.17
MS 2053.7-0449	0.583	4.7 ± 0.7	4.5 ± 0.6	5.6 ± 1.1	3.4 ± 0.6	0.32 ± 0.24	0.23 ± 0.20	0.26 ± 0.23	0.59 ± 0.41
MACS J0647.7+7015	0.584	14.9 ^{+4.5} _{-3.0}	11.7 ^{+3.6} _{-2.2}	10.7 ^{+1.7} _{-2.7}	9.5 ± 1.6	0.43 ± 0.39	0.40 ± 0.25	0.39 ± 0.22	0+0.18
RX J1120.1+4318	0.600	5.4 ± 0.4	5.2 ± 0.4	5.0 ± 0.4	4.9 ± 0.5	0.54 ± 0.10	0.51 ± 0.18	0.26 ± 0.12	0 + 0.16
MACS J0744.8+3927	0.686	5.3 ± 0.6	8.7 ± 1.7	9.0 ± 1.6	5.9 ± 0.7	0.97 ^{+0.40} _{-0.17}	0.18 ± 0.23	0.20 ± 0.18	0.24 ± 0.13
MS 1137.5+6625	0.782	7.0 ^{+1.0} _{-0.7}	7.5 ± 1.0	8.5 ± 1.4	5.6 ± 0.7	0.43 ± 0.18	0 + 0.26	0.38 ± 0.21	0.24 ± 0.13
RX J1716.9+6708	0.813	10.5 ^{+3.2} _{-2.6}	4.6 ^{+1.1} _{-0.5}	4.3 ± 0.8	N/A	0.37 ± 0.33	0.23 ± 0.21	0.88 ± 0.27	N/A
CL J1226.9+3332	0.890	12.7 ± 0.8	11.5 ± 0.8	10.9 ± 0.7	9.3 ± 0.5	0.34 ± 0.11	0.29 ± 0.11	0.08 ^{+0.11} _{-0.08}	0.06 ^{+0.13} _{-0.06}

Table 7. The eight subsets of the sample used to calculate average temperature and iron abundance profiles.

Classification of Subsets				
Subset #	Redshift	Temperature	Cooling	Number
1	$z < 0.4$	< 6.8 keV	Yes	6/6
2	$z < 0.4$	≥ 6.8 keV	Yes	4/4
3	$z < 0.4$	< 6.8 keV	No	3/3
4	$z < 0.4$	≥ 6.8 keV	No	4/4
5	$z > 0.4$	< 6.8 keV	Yes	2/2
6	$z > 0.4$	≥ 6.8 keV	Yes	2/2
7	$z > 0.4$	< 6.8 keV	No	5/3
8	$z > 0.4$	≥ 6.8 keV	No	9/7

The two values in the number column represent the number of observations and the number of unique clusters in that sample, respectively.

Table 8. General information for each cluster: the overall (defined here to be from $0 - 2r_c$) temperature and iron abundance, the overall luminosity, the total number of counts in the cluster, the calculations relevant to the cooling time, and finally the subset as defined in Table 7.

Cluster Name	Temperatures and Iron abundances for each full cluster				Cooling calculations for each central region					Analysis Subset
	z	Temperature	Iron Abundance	# of Counts	\mathcal{L}_{0-2}	$\mathcal{L}_{0-0.5}$	Proton Density	Cooling Time	Age	Subset #
Abell 1413 [†]	0.142	7.0 ± 0.3	0.46 ± 0.08	11164	5.11	1.95	0.019	3.79	8.55	2
Abell 2204 [†]	0.152	4.3 ± 0.1	0.86 ± 0.08	16382	5.17	1.09	0.22	0.24	8.44	1
Abell 665 [†]	0.182	8.0 ± 0.4	0.40 ± 0.08	12526	3.89	0.87	0.012	6.91	8.11	2
RX J0439.0+0520 [†]	0.208	3.6 ± 0.2	0.76 ± 0.17	2018	1.96	0.75	0.08	0.57	7.83	1
Abell 773	0.217	8.0 ± 0.7	0.32 ± 0.13	8351	9.24	5.24	0.0058	14.72	7.74	4
Abell 1763	0.223	7.9 ± 0.2	0.34 ± 0.04	48845	8.81	3.52	0.0062	12.93	7.68	4
Abell 2390 [†]	0.228	8.5 ± 0.2	0.43 ± 0.04	36705	10.70	3.41	0.038	1.94	7.63	2
Abell 1835 [†]	0.253	6.0 ± 0.1	0.39 ± 0.01	242214	18.20	7.20	0.088	0.71	7.38	1
Abell 697	0.282	9.7 ± 0.7	0.35 ± 0.08	13442	16.6	7.75	0.0082	11.15	7.10	4
Abell 611 [†]	0.288	7.0 ± 0.3	0.31 ± 0.06	15213	6.53	2.64	0.019	3.92	7.04	2
MS 1008.1-1224	0.306	6.3 ± 0.4	0.35 ± 0.08	7257	4.18	1.28	0.0082	8.49	6.88	3
MS 2137.3-2353 [†]	0.313	4.6 ± 0.1	0.35 ± 0.04	16958	8.29	2.87	0.10	0.60	6.81	1
Abell 1995	0.319	8.9 ± 0.5	0.28 ± 0.10	34062	15.20	5.73	0.0062	13.58	6.73	4
ZWCL 1358+6245 [†]	0.328	6.1 ± 0.3	0.39 ± 0.08	8208	3.37	0.94	0.035	1.65	6.68	1
RX J0256.5+0006	0.360	5.0 ± 0.2	0.34 ± 0.06	8608	4.49	1.36	0.0061	11.32	6.40	3
RX J0318.2-0301	0.370	5.7 ± 0.3	0.28 ± 0.08	7879	3.76	1.31	0.0064	9.16	6.32	3
RX J0426.1+1655 [†]	0.380	5.4 ± 0.4	0.19 ± 0.07	33174	1.55	0.77	0.021	2.83	6.23	1
MACS J2228.5+2036	0.412	7.1 ± 0.5	0.33 ± 0.10	6199	15.29	6.24	0.0081	10.30	5.97	8
MACS J2214.9-1359	0.483	8.8 ± 0.8	0.29 ± 0.12	3399	14.36	5.20	0.011	7.61	5.43	8
MACS J1311.0-0310 [†]	0.490	6.5 ± 0.6	0.45 ± 0.13	2111	10.57	4.60	0.021	3.09	5.38	5
MS 0015.9+1609	0.541	9.8 ± 0.6	0.28 ± 0.06	17837	23.57	3.28	0.0041	21.99	5.02	8
MACS 1423.8+2404 [†]	0.545	5.3 ± 0.1	0.54 ± 0.05	17674	10.06	3.31	0.12	0.50	4.99	5
MS 0451.6-0305	0.550	9.4 ± 0.7	0.40 ± 0.11	14303	22.11	7.34	0.011	8.32	4.96	8
MACS J2129.4-0741	0.570	7.0 ± 1.1	0.41 ± 0.23	1755	10.63	2.59	0.018	4.64	4.82	6
MS 2053.7-0449	0.583	4.9 ± 0.5	0.28 ± 0.10	1733	1.95	0.41	0.0083	7.75	4.74	7
MACS J0647.7+7015	0.584	$11.5^{+2.8}_{-2.0}$	$0.19^{+0.26}_{-0.19}$	2717	16.27	7.58	0.013	8.79	4.73	8
RX J1120.1+4318	0.600	5.2 ± 0.4	0.37 ± 0.11	10239	7.22	3.28	0.0063	11.21	4.63	7
MACS J0744.8+3927 [†]	0.686	6.8 ± 0.7	0.51 ± 0.18	1153	9.36	2.66	0.063	1.09	4.11	6
MS 1137.5+6625	0.782	7.2 ± 0.6	0.26 ± 0.13	4073	6.03	2.07	0.014	5.61	3.59	8
RX J1716.9+6708	0.813	4.6 ± 0.5	0.57 ± 0.23	1649	6.16	2.21	0.0088	9.69	3.43	7
CL J1226.9+3332	0.890	11.1 ± 0.3	0.20 ± 0.05	29846	20.56	10.06	0.014	7.42	3.07	8

The column $\mathcal{L}_{0-0.5}$ is the luminosity from $0 - 0.5r_c$, and \mathcal{L}_{0-2} is the luminosity from $0 - 2r_c$. The luminosities are in $erg - s^{-1}$, the times are in Gyr, and the densities are in units of cm^{-3} . Galaxy clusters with a dagger(†) next to them have confirmed radio sources likely associated with the cluster. The temperature and iron abundance have the same units as in Table 6.

Table 9. Average temperature as a function of counts radius, separated by redshift, temperature and cooling times. Unweighted averages are in parentheses.

Subset #	Temperatures in keV			
	Region #1	Region #2	Region #3	Region #4
1	$4.67(4.18) \pm 0.04(0.27)$	$6.51(6.38) \pm 0.07(0.63)$	$7.05(6.92) \pm 0.08(0.87)$	$7.26(7.32) \pm 0.09(1.23)$
2	$7.06(6.91) \pm 0.16(0.37)$	$8.37(8.04) \pm 0.24(0.50)$	$8.68(8.36) \pm 0.29(0.60)$	$7.51(7.45) \pm 0.24(0.92)$
3	$4.81(5.15) \pm 0.23(0.57)$	$5.54(5.55) \pm 0.31(0.11)$	$5.0(5.69) \pm 0.29(0.89)$	$4.18(5.52) \pm 0.22(0.91)$
4	$7.81(8.13) \pm 0.28(0.49)$	$8.69(9.12) \pm 0.35(0.28)$	$7.34(8.61) \pm 0.24(0.59)$	$6.90(8.15) \pm 0.24(0.57)$
5	$4.11(4.38) \pm 0.11(0.30)$	$5.81(6.26) \pm 0.18(0.49)$	$7.16(7.29) \pm 0.28(0.15)$	$6.08(5.89) \pm 0.38(1.06)$
6	$5.65(6.13) \pm 0.52(0.85)$	$7.68(7.95) \pm 0.96(0.79)$	$8.12(8.27) \pm 0.97(0.68)$	$5.56(5.55) \pm 0.51(0.31)$
7	$5.34(6.86) \pm 0.32(1.81)$	$4.93(4.78) \pm 0.33(0.23)$	$4.94(4.97) \pm 0.36(0.38)$	$4.21(2.75) \pm 0.37(1.44)$
8	$9.47(9.89) \pm 0.37(1.09)$	$9.48(9.78) \pm 0.37(0.55)$	$9.83(10.03) \pm 0.40(0.63)$	$7.90(8.18) \pm 0.29(0.63)$

Table 10. Average iron abundance as a function of counts radius, separated by redshift, temperature and cooling times. Unweighted averages are in parentheses.

Subset #	Iron Abundance in Solar Units			
	Region #1	Region #2	Region #3	Region #4
1	$0.48(0.55) \pm 0.02(0.09)$	$0.37(0.45) \pm 0.02(0.12)$	$0.27(0.30) \pm 0.02(0.05)$	$0.25(0.32) \pm 0.02(0.09)$
2	$0.42(0.42) \pm 0.04(0.03)$	$0.38(0.37) \pm 0.05(0.04)$	$0.33(0.37) \pm 0.05(0.07)$	$0.27(0.39) \pm 0.04(0.12)$
3	$0.46(0.45) \pm 0.08(0.07)$	$0.34(0.34) \pm 0.07(0.04)$	$0.28(0.27) \pm 0.06(0.05)$	$0.13(0.24) \pm 0.06(0.10)$
4	$0.44(0.43) \pm 0.06(0.04)$	$0.20(0.25) \pm 0.05(0.07)$	$0.37(0.47) \pm 0.05(0.09)$	$0.27(0.25) \pm 0.04(0.06)$
5	$0.56(0.43) \pm 0.07(0.24)$	$0.51(0.92) \pm 0.07(0.44)$	$0.32(0.22) \pm 0.05(0.13)$	$0.43(0.35) \pm 0.07(0.13)$
6	$0.66(0.71) \pm 0.19(0.26)$	$0.26(0.26) \pm 0.15(0.08)$	$0.28(0.31) \pm 0.14(0.11)$	$0.39(0.45) \pm 0.10(0.21)$
7	$0.50(0.41) \pm 0.09(0.07)$	$0.34(0.32) \pm 0.11(0.09)$	$0.34(0.47) \pm 0.10(0.21)$	$0.08(0.20) \pm 0.15(0.20)$
8	$0.47(0.47) \pm 0.06(0.05)$	$0.25(0.24) \pm 0.05(0.05)$	$0.16(0.22) \pm 0.05(0.05)$	$0.22(0.23) \pm 0.05(0.08)$